sustainability

MDPI

Article

Experimental Study on Pile Load Transfer Considering Rice Stone Filled-In Gaps between Steel Drive Pipe and Pile Casing in Karst Region

Fangcai Zhu [1,2,*], Zhijia Yang [1,2], Qing Liu [1], Yanlin Zhao [3], Binbin Wu [4], Shaolong Zhang [4], Qi Chen [4], Yifan Chen [1,2] and Rui Luo [3]

[1] School of Civil Engineering, Hunan University of Technology, Zhuzhou 412007, China
[2] Intelligent Control of Safety and Risk for Existing Engineering Structures, Key Laboratory of Hunan Province, Zhuzhou 412007, China
[3] School of Resources & Environmental and Safety Engineering, Hunan University of Science and Technology, Xiangtan 411201, China
[4] China Railway Beijing Engineering Bureau Group Second Engineering Co., Ltd., Changsha 410116, China
* Correspondence: zhufangcai@163.com

Abstract: For a guarantee of perpendicularity and stiffness in piles in Karst areas, full rotary cast-in-place piles are often utilized, steel pipes are rotarily driven into a stratum, and inner-steel pile casing is positioned. With the engineering background of the bridge piles of Guinan high-speed railway in Guangxi autonomous region, the space between steel drive pipe is filled with rice stones, the load-transfer mechanism of which was studied. An apparatus was designed for pullout of the drive pipe, rice stones are replaced with coarse stones, a simplified organic glass-pipe model is put forward, another similar indoor stratigraphic model is also pre-cast, and the movement of coarse sands and load transfer is studied with two models. The quantity of sands is calculated using back analysis through reappearance and the Rhino model: the first one is estimated using a reproduction of the pullout procedure, the second is calculated through the Rhino model based on the observation of the shape of sand in caves. When the drive pipe is pulled out, some coarse sand flows into the Karst caves and becomes loose, while load is applied on the top of the pile. The movement of coarse sand develops further, and more coarse sand flows into caves close to the bottom; this leads to a reduction its frictional resistance, and the axial force of the pile increases closer to the upper position of the cave, whereas the axial force of the pile is concentrated almost constantly close to the bottom of the cave. Comparing the end resistance and the frictional resistance, coarse sand can bear pile load to a great extent.

Keywords: Karst caves; rice stone; full rotary cast-in-place pile; steel drive pipe; steel pile casing; axial force of a pile

Citation: Zhu, F.; Yang, Z.; Liu, Q.; Zhao, Y.; Wu, B.; Zhang, S.; Chen, Q.; Chen, Y.; Luo, R. Experimental Study on Pile Load Transfer Considering Rice Stone Filled-In Gaps between Steel Drive Pipe and Pile Casing in Karst Region. *Sustainability* **2023**, *15*, 14659. https://doi.org/10.3390/su152014659

Academic Editor: Jianjun Ma

Received: 3 August 2023
Revised: 12 September 2023
Accepted: 13 September 2023
Published: 10 October 2023

1. Introduction

In Karst locations, full rotary cast-in-place piles are frequently employed. A pipe is utilized to follow up drilling to prevent the collapse of the pile hole. The casing is fitted with a steel pipe to make pouring concrete easier, and fill in gaps between the steel drive pipe and pile casing so that the piles remain solid and vertical. The fully casing rotary construction method is safe, low-polluting, highly efficient, and has less impact on the pile's perimeter, making it an excellent way to ensure the pile's quality and boost its bearing capacity [1–3]. Igoe D et al. used cased bored piles in soft soils, and they performed better with a tensile static load than ordinary bored piles [4]. The use of full casing cast-in-place piles during the construction process can reduce the lateral displacement of the pile, according to research by Gao G et al. [5]. By studying three different types of piles in the field, Zhou et al. discovered that the pile axial-force decay rate increased with the

pile lateral resistance [6]. The verticality of the casing is a key factor in the control of the pile bearing performance and is mostly controlled by verticality control frames, which are then calibrated with a theodolite [7–9]. Hong points out that in order to stabilize the inner casings, prevent the pile from deviating, and enhance the rigidity of the casings [10], the gap between the inner and outer casings is typically filled; this may make it challenging to remove the outer casings. Using an indoor model test, Gao et al. conducted a study of the load transfer law of a driven cast-in-place pile through multi-layered cavities and revealed that the axial force of the pile decreases with the position of the Karst cave [11]. Huang et al. conducted numerical simulations on the effect of pile foundations through beaded caverns on its load transfer law and revealed that there is a section of pile side friction that rapidly attenuates at the free surface of the cavern roof, but that this section changes little as the external load increases to a certain level [12]. The bearing capacity of the pile end in a multi-cavity stratum was examined by Liang et al., who concluded that it declined as the cavity diameter increased [13]. By computationally simulating variables such as cavity length, height, and top-plate thickness, Wang et al. investigated the impact of cavities on the bearing capacity of super-long pile foundations and concluded that the cavities had little impact on the pile foundations' dynamic response [14]. In numerical simulations of cavern span variations on the bearing characteristics of bridge pile foundations, Feng et al. discovered that the pile side friction resistance tends to decrease with increasing cavern span [15]. Zhou et al. found that the pile axial force curve at the cavity was concave by simulating the axial force transfer law through the cavity at different heights [16]. Mei et al. designed and proposed a new type of cast-in-place pile to address the problem that piles cannot be formed in the Karst region due to cavities [17]. Increasing the height, span, and number of caves harmed the bearing capacity of pile foundations, according to research by Chen et al. on pile foundations through caves [18]. Gotman N Z et al. proposed a method to calculate the numerical variation of shear stresses on the lateral surface of piles at various stages of loading by analyzing the extra loads placed on the piles during the formation of cavities [19]. Xu et al. divided the entire settlement process into three parts after analyzing the axial load-settlement law of bored piles containing debris [20]. Using static load testing of pile foundations in karst areas, He et al. proposed a method for calculating the vertical bearing capacity of pile foundations based on the load-transfer method [21]. A method to determine the critical load for pile buckling when navigating a single-level cavern was put forth by Lei et al. after conducting indoor model experiments [22]. Using numerical simulation tools, Liang et al. carried out orthogonal tests and concluded that the location and size of the cavity had a substantial impact on the pile's eventual lateral bearing capacity [23].

In the background of the construction of full rotary cast-in-place piles for the Guinan high-speed railway in the Guangxi autonomous region, the rice stones are inserted between the steel drive pipe and the pile casing when the pile foundation crosses many cavities, which solves the problem of the rapid attenuation of pile-side friction resistance at the free surface of the karst cave roof in traditional full rotation cast-in-place piles and ensures the verticality of the pile body. This is to study the movement pattern of rice stone and the effect of filled rice stone on the pile load transfer when the casing is pulled out and the pile top is loaded.

2. Project Overview

The Baxian double-track super-large Bridge of the Guinan High-Speed Railway is a Karst landscape with a total length of 7294 m in Chengjiang Town, Du'an County, Guangxi. The caves discovered at the karst were more developed at the pier pile and the caves were distributed in a series of beads, as shown in Figure 1. The pile lengths ranged from 14.5 m to 77 m. Through multiple impacts of the impact drill, ground collapse, hole collapse, and other situations occur, making hole formation difficult. The fully casing rotary construction technology was employed to assure the quality and efficiency of the pile formation. The drill bit and steel casing were selected according to

the design hole diameter. For pile foundations with a design diameter of 1.25 m, a drill bit and steel casing with an internal diameter of 1.4 m were used, and for pile foundations with a design diameter of 1.5 m, a drill bit and steel casing with an internal diameter of 1.6 m were used. The steel casing's wall thickness was 5 cm. Steel sheaths were installed around the pile's perimeter to prevent concrete from flowing into the cavity as it formed the pile. For pile foundations with 1.5 m diameter holes, steel casings with inner diameters of 1.5 m and 2 cm each were used, and for pile foundations with 1.25 m diameter holes, steel casings with inner diameters of 1.25 m and 2 cm each were used.

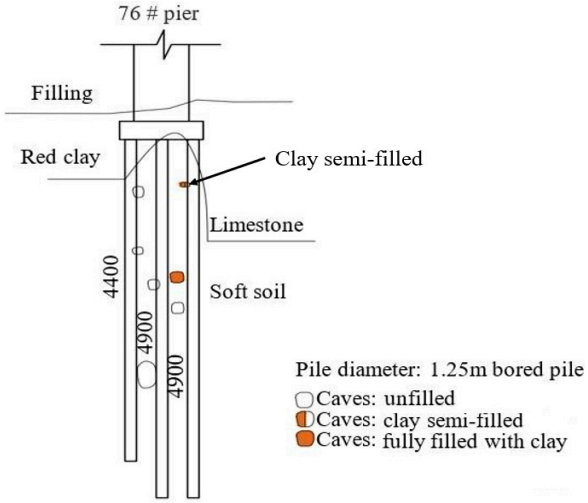

Figure 1. Pile foundation for 76#.

To ensure the verticality of the pile, the gap between the steel pipe and pile casing was filled with rice stone with a grain size of no more than 5 mm. The construction procedure is depicted in Figure 2. There are two types of filling for rice stones: one is filling before the steel casing is pulled out, and the other is filling after the steel casing is pulled out. The former filling type is more effective at controlling verticality, but in the latter filling type, it is easier to pull out the steel casing. This paper focuses on the indoor experimental study of the first filling method.

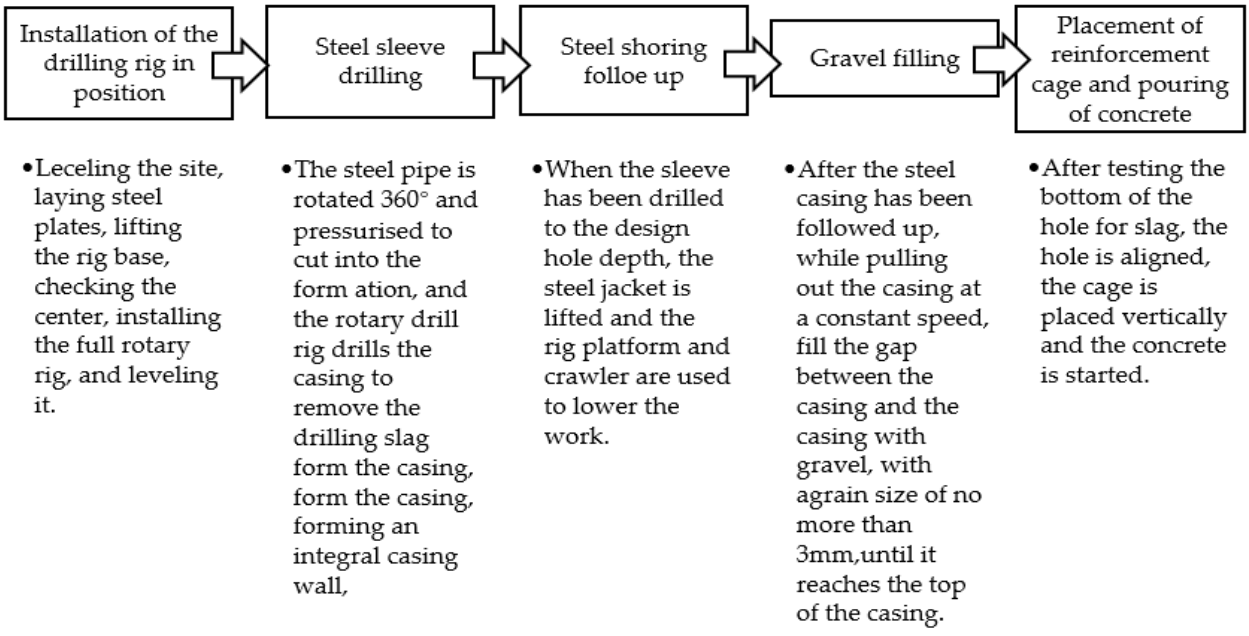

Figure 2. Construction technology of full rotary cast-in-place pile.

3. Experimental Scheme

To analyze the characteristics of coarse sand inflow into the cavity and load transfer when the casing is pulled out and the pile top is loaded, two models were used for indoor experimental simulations: the simplified model of a Plexiglas tube and a similar model of a double-layer Karst pile foundation. The aim is to discover whether the pile perimeter within the extent of the cavity contains soil for comparative analyses. These models were used to fill the gap between the steel pipe and pile casing, with 1.18~2.36 mm coarse sand rather than on-site rice stone.

3.1. Indoor Experimental Models

3.1.1. Plexiglass Tube Simplified Model

The simplified model of the plexiglass tube is shown in Figure 3, with the soil layer on the pile side is replaced by plexiglass tube. The base was 700 × 700 × 300 mm in size, was made of M2.5 cement mortar, and the ratio of cement/river/sand/water = 1:6.29:1.48. An integrated model was created that included both the pile's perimeter and the cavity. The model was 10 cm deep in the base. The elastic modulus of the transparent plexiglass tube was 3.15 Gpa [24]. The plexiglass tube had an inner diameter of 79 mm, a wall thickness of 5 mm, and a height of 750 mm. According to Figure 4, the casing was constructed of white PVC tubing with an outer diameter of 75 mm, an inner diameter of 70.4 mm, and a height of 800 mm. The model pile was constructed from a circular, hollow piece of UPVC with an outer diameter of 50 mm, a wall thickness of 3.7 mm, a 3 GPa elastic modulus, and a pile length of 750 mm. The strain gauges were symmetrically affixed to the inner wall of the half-sectioned UPVC pipe and then pasted into the entire pile using epoxy resin to safeguard them and make testing easier, as illustrated in Figures 5 and 6. To mimic the cavities, a circular horizontal layout was used. Cavities no. 1 and no. 3 had an exterior diameter of 30 mm, an inner diameter of 20 mm, and a length of 70 mm, and the acceptable amount of sand for these was 28.35 g, whereas cavities no. 2 and no. 4 had an outward diameter of 40 mm, an inner diameter of 30 mm, and a length of 70 mm, and the acceptable amount of sand for these was 63.8 g. One strain gauge was placed at the upper and bottom margins of the hollow, while at other points, two strain gauges were placed symmetrically.

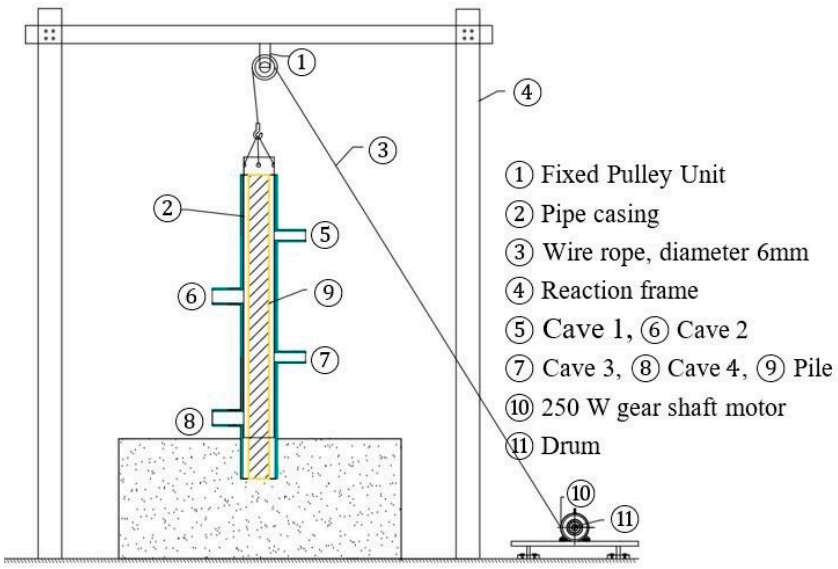

Figure 3. Simplified model of organic glass pipe.

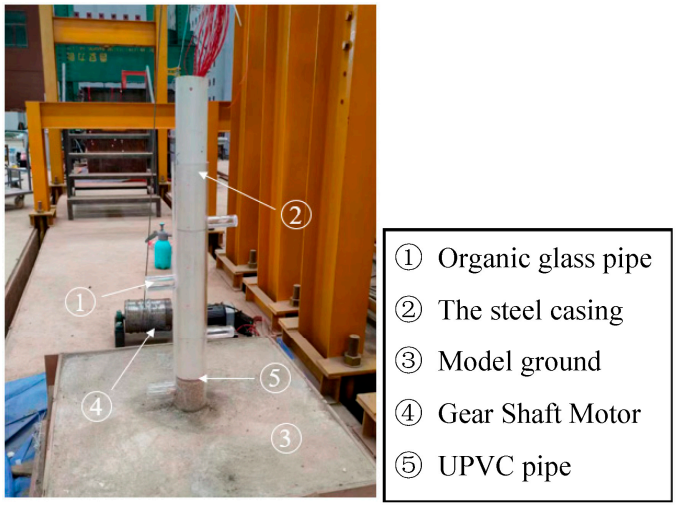

Figure 4. Simplified model test device for organic glass pipe.

Figure 5. Model pile strain gauge pasting.

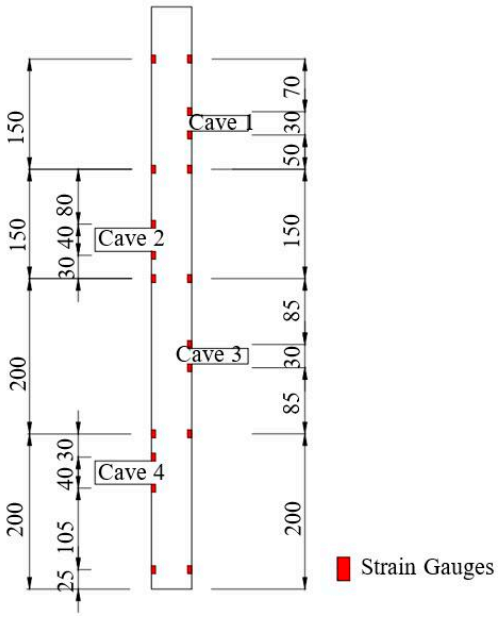

Figure 6. Layout of caves and strain gauges in simplified model of organic glass pipe.

3.1.2. Similarity Model of Double Strata Batholith

Combined with the engineering practice, the influence of limestone overlying soil on the test results was considered [25–35]. A similar model of double-layer Karst pile foundation is shown in Figure 7. The upper layer was 165 mm thick covering soil, and the lower portion was 760 mm thick limestone. Similar materials are often used for simulation in rock mechanics tests [36–39]. It is poured into an 800 × 800 × 1200 mm steel model box. Sand, cement, and gypsum powder are combined in a ratio of 6:0.7:0.3 to create a cement–gypsum mortar composition that mimics limestone [40]. It was poured in two times. The model pile was buried 100 mm below the surface of the bedrock and maintained for 24 h. The casing was manufactured from white PVC pipe with an exterior diameter of 75 mm, an inner diameter of 70.4 mm, and a length of 800 mm after being poured in five layers of 100 mm each. It was vibrated and brushed, and it was maintained in place for 28 days after completion.

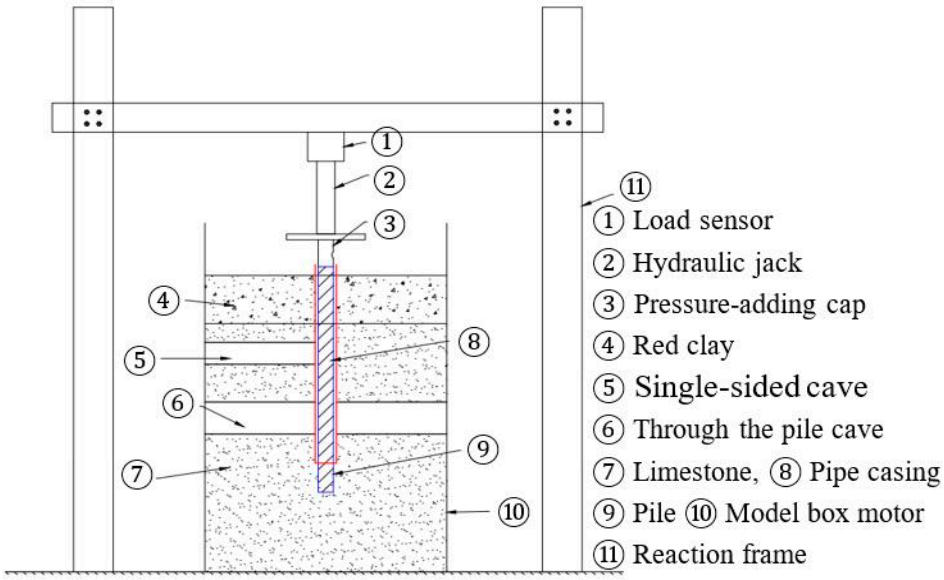

Figure 7. Similar model of double-stratum Karst pile foundation.

The soils were red clay, taken from near the test site, with the parameters shown in Table 1. To make sure that the soil layer was formed, a boundary of a steel model frame measuring 750 × 750 × 300 mm was set. Three layers of 50 mm, 50 mm, and 65 mm of soil were compacted. The soil was covered with plastic film for 24 h after filling, and the level of compaction was kept at 91%, as shown in Figure 8.

The model pile was made of the same material as that in the plexiglass simplified model test. The strain gauge arrangement and cavities are shown in Figure 9. The diameter of the cavity on one side was 75 mm, 260 mm from the pile's top, and its acceptable amount of sand was 2064.86 g; the diameter of the cavity through the pile was 110 mm, 465 mm from the pile's top, and its acceptable amount of sand was 8883.47 g. To analyze the characteristics of coarse sand flowing into the cavity during pipe pulling and loading, the length of the cavity extended to the model border. At the upper, middle, and lower margins of the cavity, strain gauges were placed, and two strain gauges were placed symmetrically in other places.

Table 1. Physical–mechanical properties of filled soil.

Water Content ω (%)	Density ρ (g/cm^3)	Specific Gravity of Particles Gs	Cohesion c (kPa)	Angle of Internal Friction φ (°)	Maximum Dry Density ρ_{dmax} (g/cm^3)
11.45	1.81	2.64	24.24	27.92	1.78

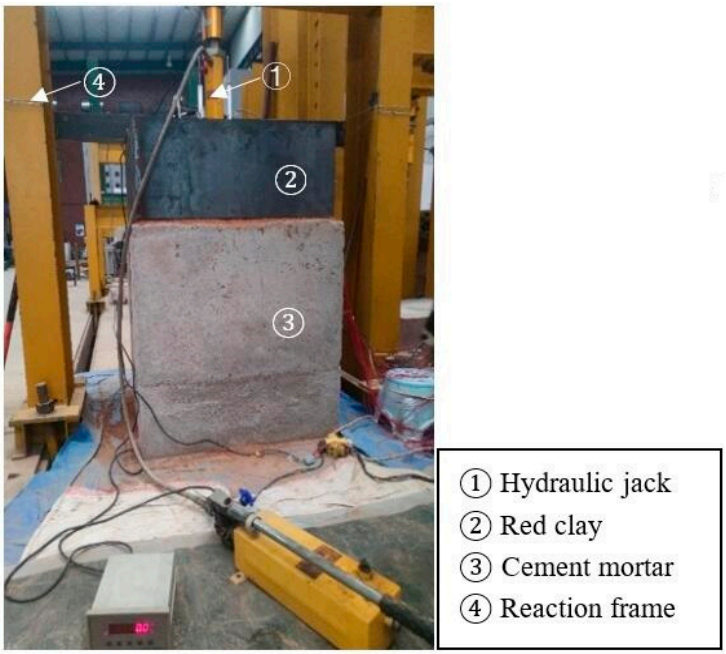

Figure 8. Loading device for similar model of double-stratum karst pile foundation.

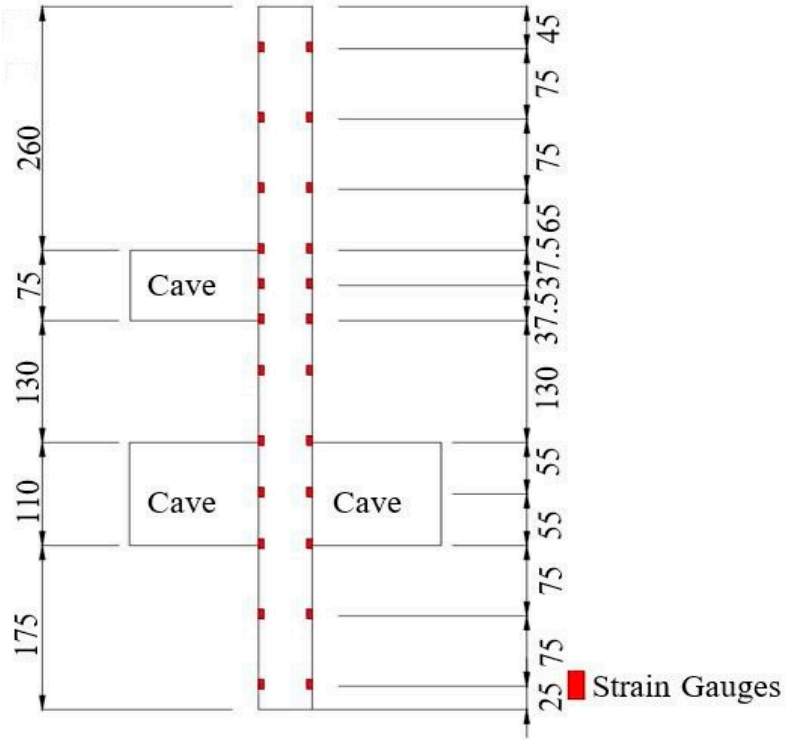

Figure 9. Layout of caves and strain gauges in similar model of double-stratum Karst pile foundation.

3.2. Test Device

The self-made pipe pulling device was designed. Through the integrated motor device consisting of a reaction frame, motor and hook, the motor speed was controlled to control the expansion and contraction of the steel wire rope and, thus, the rising speed of the casing, as shown in Figure 10. The motor was a 250 W gear-shaft motor with a maximum speed of 8 r/min and a stepless speed-change capability through the regulator (brand: Oubang, origin: Yancheng, Jiangsu). The steel wire rope was secured to the drum, which was connected to the motor by a connection. The motor speed was set to 1.2 r/min. When pulling out the pipe, sand was filled between the casing and the pile body, until the casing was pulled out, and the sand was filled to the surrounding of the pile top.

Figure 10. Pipe pull-out device.

4. Analysis of Test Results

4.1. Analysis of Coarse Sand Flow into Caves

4.1.1. Analysis of Coarse Sand Inflow in a Simplified Model of a Plexiglas Tube

The quality of sand inflow into the cavern during the process of pipe pulling was analyzed three times, and the average value was taken three times. Using photographs, the distribution pattern of coarse sand in the cavern following pile loading was examined. It was inversely derived by simulating its pile shape under conditions of no loading. Under the conditions, inversion of the pile shape was simulated to obtain its quality, and the average value of the three simulations was also taken. Figures 11 and 12 show the comparison of sand inflow in the cavity between the actual and simulated extraction of the no. 2 cavity. Tables 2 and 3 show the quality of coarse sand in the cavities after casing extraction and loading, respectively. As can be observed, the larger diameter cavities receive more sand intake, whereas the cavity closest to the pile's base receives substantially more coarse sand inflow. The inflow of coarse sand into the cavity is greater during the uplift process because the coarse sand primarily moves downwards by gravity. In contrast, when the pile is under the top load, it primarily depends on the downward driving effect of the pile side sand when the pile settles, with less relative space and a less pronounced movement trend, and the inflow of coarse sand is lesser.

Figure 11. Sand heap shape of No. 2 Karst cave after pipe pull out.

Figure 12. Sand heap shape-simulation diagram of No. 2 Karst cave after pipe pull out.

Table 2. Quantity of sand in Karst cave after pipe pulling (Simplified Model of a Plexiglas Tube).

	Simulation 1	Simulation 2	Simulation 3	Average Value (g)
Cave 1	3.38	3.32	3.94	3.55
Cave 2	12.72	12.05	12.86	12.54
Cave 3	4.8	4.86	4.52	4.80
Cave 4	14.30	13.81	13.73	13.95

Table 3. Quantity of sand in Karst cave after loading (Simplified Model of a Plexiglas Tube).

	Simulation 1	Simulation 2	Simulation 3	Average Value (g)
Cave 1	8.67	9.66	9.93	9.42
Cave 2	18.59	17.56	16.45	17.53
Cave 3	6.25	6.95	7.04	6.75
Cave 4	16.04	17.19	18.53	17.25

4.1.2. Analysis of Coarse Sand Inflow in a Similar Models for Double-Stratified Karst Pile Foundations

The volume of the sand was computed using Rhino 7 software for 3D modeling to depict the shape of the sand accumulation in the cavern, and the shape of the sand distribution in the cavern was evaluated using pictures to roughly estimate its size. The minimum dry density of 1.29 g/cm^3 was chosen for the sand density, and the mass of sand

in the cavern was calculated, as shown in Figure 13. After the extraction was finished, it was discovered that cavity No. 1, which was nearer the top of the pile, had less coarse sand mass than cavities No. 2 and 3. This is similar to the Plexiglas simplified model, as shown in Table 4. When the top of the pile was loaded, the amount of coarse sand that had accumulated in the gaps at every subsequent level was recorded. As indicated in Table 5, in which it has similar characteristics to the simple model of the plexiglass, it was discovered that the amount of coarse sand increased substantially more in cavity no. 1 towards the top of the pile and less in cavities no. 2 and no. 3 near the bottom of the pile.

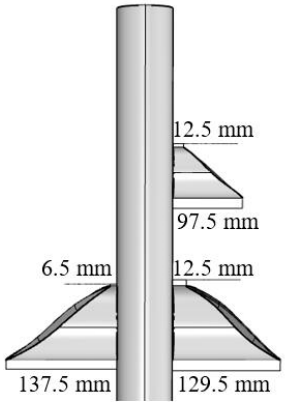

Figure 13. Sand-heap shape of Karst cave after pipe pull out.

Table 4. Quantity of sand in Karst cave after pipe pulling (Similar Models of Double-Stratified Karst Pile Foundations).

Cave	Quality (g)
Cave 1	508.6
Cave 2	1118.7
Cave 3	1198

Table 5. Quantity of sand in Karst cave after loading (Similar Models of Double-Stratified Karst Pile Foundations).

Cave	Quality (g)
Cave 1	665.4
Cave 2	1191.3
Cave 3	1245.5

4.2. Plexiglas Simplified Model Settlement and Load Transfer Analysis

4.2.1. Settlement Analysis

The load–settlement curve is shown in Figure 14, and is basically linear. When a load of 25 kN was applied, the upper pile's side frictional resistance reached its peak, the lower pile gradually picked up the load, and the settlement of the lower pile slightly increased due to compression. When the design load of 50 kN was reached, there was no obvious inflection point, the top of the pile could no longer bear the load, the pile was bent and deflected under pressure, and the pile showed buckling and instability, as shown in Figure 15.

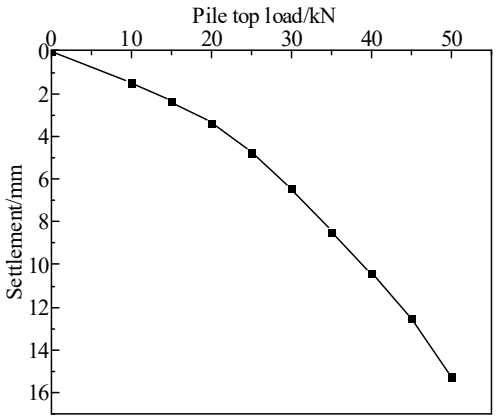

Figure 14. Load–settlement curve (Simplified Model of a Plexiglas Tube).

Figure 15. Instability of model pile (Simplified Model of a Plexiglas Tube).

4.2.2. Axial force Analysis of Pile Shaft

The axial force of the pile body at the cross-section was calculated using the following formula:

$$Q_i = \overline{\varepsilon_i} E_i A_i \quad (1)$$

where Q_i is the axial force at section i of the pile body, $\overline{\varepsilon_i}$ is the average value of the strain at section i, E_i is the modulus of elasticity of the pile body material at section i, A_i is the cross sectional area of the pile at section i.

The axial force distribution of the pile body was determined using the strain gauges placed within the pile body, although the no. 3 cave's strain gauges malfunctioned. As shown in Figure 16, the axial force became larger at the cave, and increased with the increase in the pile top load. The axial force of the pile body increased greatly at the upper part of the cave, because the coarse sand flowed into the cave near the upper part of the cave, and the sand was relatively loose, presenting the 'Void' effect. Therefore, the frictional resistance of the pile side was small, and the axial force of the pile body increased instead. It presented characteristics of 'negative frictional resistance', while the axial force of the pile body at the lower part of the cave had little change due to the 'lifting' effect of the pile side at the lower part of the cave.

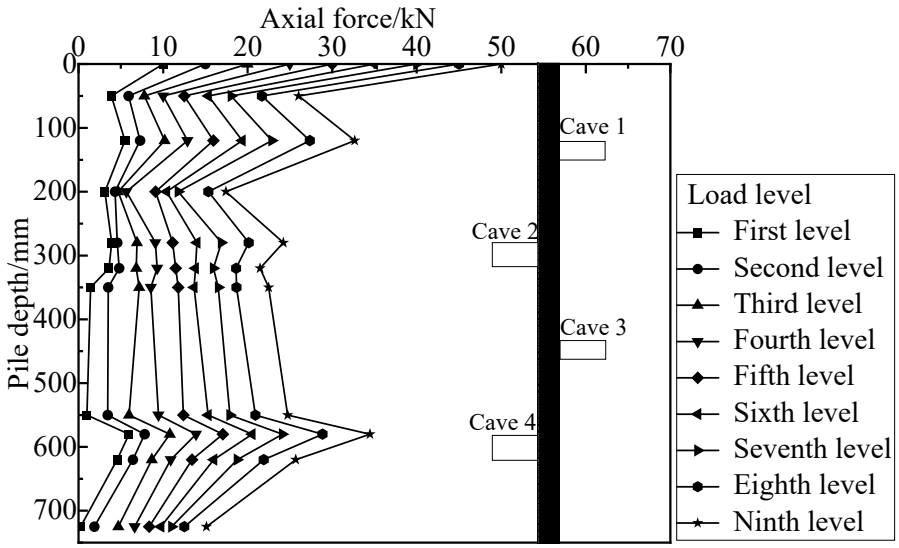

Figure 16. Distribution curve of axial force along depth (Simplified Model of a Plexiglas Tube).

4.2.3. Distribution of Pile Side Friction and Pile Tip Resistance

The layered lateral resistance and pile end resistance of the soil on the pile side was calculated using the following formulae, respectively:

$$q_{si} = \frac{Q_i - Q_{i+1}}{ul_i} \tag{2}$$

$$q_p = \frac{Q_n}{A_0} \tag{3}$$

where q_{si} is the lateral resistance between section i and section $i + 1$ of the pile, and q_p is the pile end resistance.

The distribution of the pile side friction and end resistance at various levels of loading is depicted in Figure 17 and Table 6, respectively. The majority of the pile top load was first supported by the side friction resistance. The side friction resistance increased somewhat and the percentage lowered as the weight increased. When loading reached its latter stages, the side friction resistance gradually decreased from 98% to 70% of the pile top load as the pile end started to bear the load.

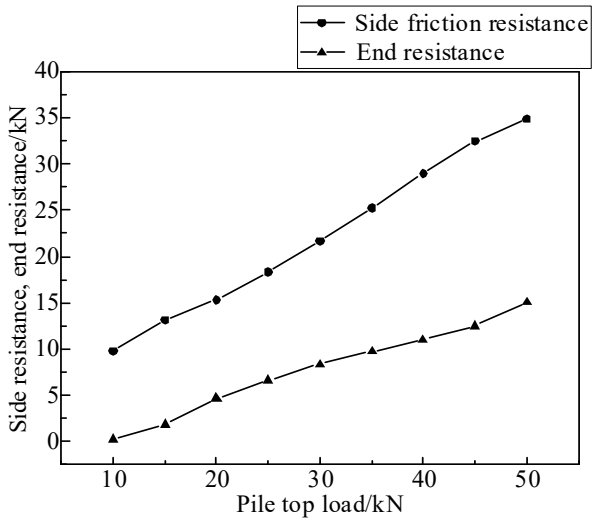

Figure 17. Distribution of end bearing friction and side friction (Simplified Model of a Plexiglas Tube).

Table 6. Proportion of pile side friction resistance (Simplified Model of a Plexiglas Tube).

Pile Top Load Q (kN)	Pile Side Friction Q_S (kN)	Q_S/Q
10	9.76	0.98
15	13.13	0.88
20	15.29	0.76
25	18.36	0.73
30	21.64	0.72
35	25.26	0.72
40	28.98	0.72
45	32.48	0.72
50	34.88	0.70

4.3. Settlement and Load Transfer Analysis of Similar Models for Double-Stratified Karst Pile Foundations

4.3.1. Settlement Analysis

The load–settlement curve is shown in Figure 18. The load was intended to be 5 kN at each level, but it was discovered that the pile settlement was too great when the pile was loaded at the first stage. As a result, the test method was changed to 2.5 kN at each stage, and the pile settlement was about linear. When the pile was loaded to 25 kN, the pile was bent and deflected near the top of the pile, and the pile was unstable at this time, as shown in Figure 19.

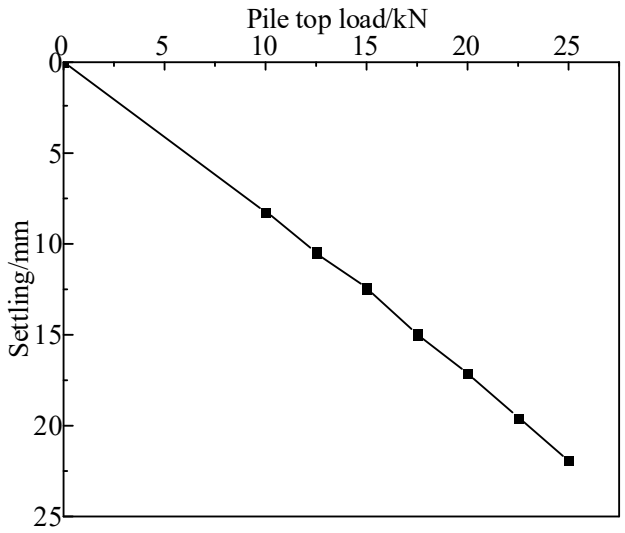

Figure 18. Load–settlement curve (Similar Models of Double-Stratified Karst Pile Foundations).

① Position before destruction
② Position after destruction

Figure 19. Instability of model pile (Similar Models of Double-Stratified Karst Pile Foundations).

4.3.2. Axial Force Analysis of Pile Shaft

The axial force of the pile body is shown in Figure 20. Along the pile's depth, the axial force decreased; nevertheless, the curve of the axial force was slightly slowed down at the interface between the clay layer and the limestone. When the pile body entered the interface of the limestone, the side frictional resistance increased compared with that at the soil layer. Similar to the simplified model of the plexiglass tube, the axial force of the pile body increased slightly on the upper side close to the cavity and barely changed on the lower side. The axial force of the pile at the cavity increased relatively slowly and had less of an impact on the change in the pile's axial force when the cavity was close the bottom of the pile.

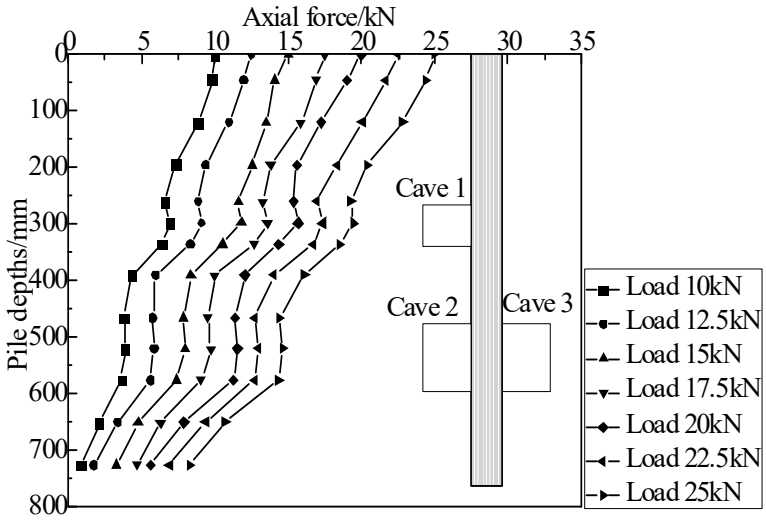

Figure 20. Distribution curve of axial force along depth (Similar Models of Double-Stratified Karst Pile Foundations).

4.3.3. Analysis of Pile Side Friction and Pile Tip Resistance

The changes in pile side friction and pile end resistance are shown in Figure 21 and Table 7. With increasing load, both pile side friction and pile end resistance increased. The pile side friction plays a major role when the pile top load is small. With the increase in load, the proportion of pile end bearing load increased, and the pile end resistance lagged behind the side friction.

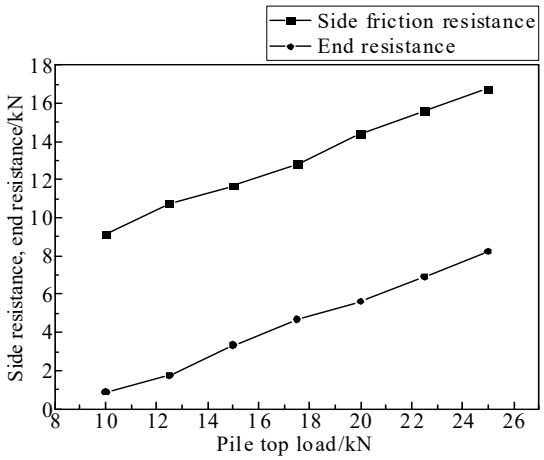

Figure 21. Distribution of end bearing friction and side friction (Similar Models of Double-Stratified Karst Pile Foundations).

Table 7. Proportion of pile side friction resistance (Similar Models of Double-Stratified Karst Pile Foundations).

Pile Top Load Q (kN)	Pile Side Friction Q_S (kN)	Q_S/Q
10	9.11	0.91
12.5	10.76	0.86
15	11.67	0.78
17.5	12.82	0.73
20	14.38	0.72
22.5	15.59	0.69
25	16.75	0.67

5. Conclusions

This article investigated the filling of rice stones between the steel drive pipe and the pile casing when the pile foundation crossed many cavities, to study the movement pattern of rice stone and the effect of filled rice stone on the pile load transfer when the casing was pulled out and the pile top was loaded. The following conclusions are drawn:

(1) A pull-out test rig was designed to simulate the casing pull-out process.
(2) The quality of coarse sand inflow into the cavity was reproduced using simulated pull-out and image analysis, and the leakage amount of the casing pull-out and pile top loading was analyzed. More sand entered the cavity closer to the pile bottom during the pull-out process, while less sand entered during the loading phase, and the sand inflow was determined by gravity and pile settlement.
(3) Near the upper side of the hole, the axial force of the pile increased, while there was less change near the lower side.
(4) Sand filling between steel casing and steel sheath increased the pile side friction resistance, improved the bearing capacity of the pile foundation, and ensured the verticality of the pile body. Improve the porosity rate during the construction process and reduce construction costs.

Author Contributions: F.Z.: conceptualization, methodology, supervision, writing—Review and Editing; Y.Z.: writing—original draft; Q.L.: investigation, writing—original draft; Z.Y.: writing—review and editing; B.W.: resources; S.Z.: resources; Q.C.: resources; Y.C.: writing—original draft; R.L.: writing—original draft. All authors have read and agreed to the published version of the manuscript.

Funding: This research is sponsored by Zhuzhou joint project of Hunan Provincial Natural Science Foundation (No. 2022JJ50087).

Data Availability Statement: All data and models generated or used during the study appear in the submitted article.

Conflicts of Interest: The authors declare no conflict of interest.

References

1. Liu, C.X. Research and application status of complete set of pipe cast-in-place pile in China. *Guangdong Archit. Civ. Eng.* **2021**, *28*, 62–66.
2. Liu, L.Y. Construction of full-set rotary bored pile in Karst Geology. *House* **2021**, *41*, 66–69.
3. Liu, J.H. Full-Rotation rapid construction technology of bored piles in Complex Karst. *Technol. Innov. Appl.* **2019**, *09*, 161–162+166.
4. Igoe, D.; Spagnoli, G.; Doherty, P.; Weixler, L. Design of a novel drilled-and-grouted pile in sand for offshore oil&gas structures. *Mar. Struct.* **2014**, *39*, 39–49. [CrossRef]
5. Gao, G.; Zhuang, Y.; Wang, K.; Chen, L. Influence of Benoto bored pile construction on nearby existing tunnel: A case study. *Soils Found.* **2019**, *59*, 544–555. [CrossRef]
6. Zhou, Z.; Yang, T.; Fan, H. A Full-Scale Field Study on Bearing Characteristics of Cast-in-Place Piles with Different Hole-Forming Methods in Loess Area. *Adv. Civ. Eng.* **2019**, *2019*, 1450163. [CrossRef]
7. Zhuang, Y.; Mou, F.; Cui, X.Y.; Zhang, H.X. Application of Benoto pile in Concealed Bridge piled project near Subway. *Chin. J. Geotech. Eng.* **2015**, *37*, 41–45.

8. Zhang, G.C. Construction of pile foundation by steel casing for follow up method in Karst StratUm with Large Cave. *J. Munic. Technol.* **2013**, *31*, 87–90.
9. Tan, Z.W. Pile foundation construction technology of steel casing follow-up method in Complex Karst Geology. *Transpo World* **2017**, *24*, 101–102.
10. Hong, H.J. River pile foundation construction technology of Spanning Bridge in Beaded Karst Cave geological condition. *Eng. Technol. Res.* **2021**, *6*, 41–42.
11. Gao, Q.; Zhang, H.C. Experimental study on load transfer law of cast-in-place pile on Multi-Layer Karst Cave. *J. China Foreign Highw.* **2021**, *41*, 40–43.
12. Huang, M.; Zhang, B.Q.; Chen, F.Q.; Huang, Z.J.; Zhang, X.D. Numerical calculation of load transfer progress of pile foundation in Beaded Karst Cave stratum. *J. Eng. Geol.* **2017**, *25*, 1574–1582.
13. Liang, G.T.; Deng, L.M.; Xiao, M.Z.; Xiao, K.Q.; He, L. Lower bound limit element analysis on bearing capacity of pile foundation above Karst Caves. *J. Yangtze River Sci. Res. Inst.* **2022**, *37*, 94–99.
14. Wang, P.; Ding, H.; Zhang, P. Influence of Karst Caves at Pile Side on the Bearing Capacity of Super-Long Pile Foundation. *Math. Probl. Eng.* **2020**, *2020*, 4895735. [CrossRef]
15. Feng, Z.; Chen, J.; He, J.; Huang, Z.; Dong, Y.; Jiang, D.; Meng, Y. Study on Vertical Bearing Characteristics of Bridge Pile Foundation in Karst Area Considering the Size. *IOP Conf. Ser. Mater. Sci. Eng.* **2020**, *780*, 022003. [CrossRef]
16. Zhou, D.Q.; Zhang, Y.L.; Cao, Y.; Zhang, H.C.; Xie, R.T.; Du, P. Experiment on the effect of Karst Cave height on axial force transfer of rock-socketed piles and the response to pile side overload. *J. Hunan Univ.* **2022**, *49*, 83–93.
17. Mei, G.X.; Lu, Z.Y.; Chen, J.X.; Zhang, F.Y.; Yang, J.M.; Jiang, M.J. Research on the bearing mechanism of a new type grouted pile in Karst Area. *J. Hunan Univ.* **2022**, *49*, 32–44.
18. Chen, H.Y.; Feng, Z.J.; Li, T.; Bai, S.F.; Zhang, C. Study on the vertical bearing performance of pile across cave and sensitivity of three parameters. *Sci. Rep.* **2021**, *11*, 17342. [CrossRef]
19. Gotman, N.Z.; Evdokimov, A.G. Determination of additional load on the bridge foundation pile under karst deformation. *J. Phys. Conf. Ser.* **2021**, *1928*, 012058. [CrossRef]
20. Xu, M.J.; Ni, P.P.; Mei, G.X.; Zhao, Y.L. Load-settlement behaviour of bored piles with loose sediments at the pile tip: Experimental, numerical and analytical study. *Comput. Geotech.* **2018**, *102*, 92–101. [CrossRef]
21. He, Q.; Yu, Z.; Yue, W.; Tan, W.; Li, Z. Algorithm for Vertical Bearing Capacity Calculation of Rock-Socketed Piles in Karst Area Based on Load Transfer Method. *IOP Conf. Ser. Earth Environ. Sci.* **2021**, *719*, 042073. [CrossRef]
22. Lei, Y.; Li, P.J.; Liu, Z.Y.; Wang, H.; Peng, P.; Xu, H. Calculation method and experimental study of critical buckling load of foundation piles crossing karst caves in karst areas. *Geotech. Mech.* **2022**, *43*, 3347–3356.
23. Liang, J.-H.; Fan, Q.-Y.; Qin, K. Influence of Karst Caves on the Pile's Bearing Characteristics-A Numerical Study. *Front. Earth Sci.* **2022**, *9*, 754330. [CrossRef]
24. Shi, J.H. Determinaton of dynamic elastic modulus of Plexiglass. *J. Suzhou Coll. Educ.* **1996**, *13*, 83–84.
25. Zhao, Y.; Luo, S.; Wang, Y.; Wang, W.; Zhang, L.; Wan, W. Numerical Analysis of Karst Water Inrush and a Criterion for Establishing the Width of Water-resistant Rock Pillars. *Mine Water Environ.* **2017**, *36*, 508–519. [CrossRef]
26. Liu, S.; Nie, Y.; Hu, W.; Ashiru, M.; Li, Z.; Zuo, J. The Influence of Mixing Degree between Coarse and Fine Particles on the Strength of Offshore and Coast Foundations. *Sustainability* **2022**, *14*, 9177. [CrossRef]
27. Li, Y.; Zeng, X.; Lin, Z.; Su, J.; Gao, T.; Deng, R.; Liu, X. Experimental study on phosphate rock modified soil-bentonite as a cut-off wall material. *Water Supply* **2022**, *22*, 1676–1690. [CrossRef]
28. Liu, Y.; He, B.; Xie, J.; Lu, Y.; Zhang, L. Compatibility of geosynthetic clay liners at different temperatures. *J. Environ. Prot. Ecol.* **2022**, *22*, 2295–2306.
29. Yu, S.; Chen, Y.; Zhao, J.; Fu, S.; Li, Z.; Xia, H.; Zhou, L. Temperature sensitivity of total soil respiration and its heterotrophic and autotrophic components in six vegetation types of subtropical China. *Sci. Total Environ.* **2017**, *607–608*, 160–167. [CrossRef]
30. Chen, C.; Peng, Z.; Gu, J.; Peng, Y.; Huang, X.; Wu, L. Exploring Environmentally Friendly Biopolymer Material Effect on Soil Tensile and Compressive Behavior. *Int. J. Environ. Res. Public Health* **2020**, *17*, 9032. [CrossRef]
31. Feng, T.; Chen, H.; Wang, K.; Nie, Y.; Zhang, X.; Mo, H. Assessment of underground soil loss via the tapering grikes on limestone hillslopes. *Agric. Ecosyst. Environ.* **2020**, *297*, 106935. [CrossRef]
32. Zhang, Y.; Ren, B.; Hursthouse, A.S.; Deng, R.; Hou, B. An Improved SWAT for Predicting Manganese Pollution Load at the Soil-Water Interface in a Manganese Mine Area. *Pol. J. Environ. Stud.* **2018**, *27*, 2357–2365. [CrossRef] [PubMed]
33. Xie, Q.; Ren, B.; Hursthouse, A.; Shi, X. Effects of mining activities on the distribution, controlling factors, and sources of metals in soils from the Xikuangshan South Mine, Hunan Province. *Integr. Environ. Assess. Manag.* **2022**, *18*, 748–756. [CrossRef] [PubMed]
34. Zhou, T.; Luo, X.; Hou, Y.; Xiang, Y.; Peng, S. Quantifying the effects of road width on roadside vegetation and soil conditions in forests. *Landsc. Ecol.* **2020**, *35*, 69–81. [CrossRef]
35. Luo, X.; Ren, B.; Hursthouse, A.S.; Thacker, J.R.; Wang, Z. Soil from an abandoned manganese mining area (Hunan, China): Significance of health risk from potentially toxic element pollution and its spatial context. *Int. J. Environ. Res. Public Health* **2020**, *17*, 6554. [CrossRef] [PubMed]
36. Chen, W.; Wan, W.; Zhao, Y.; Peng, W. Experimental Study of the Crack Predominance of Rock-Like Material Containing Parallel Double Fissures under Uniaxial Compression. *Sustainability* **2020**, *12*, 5188. [CrossRef]

37. Wu, H.; Jia, Q.; Wang, W.; Zhang, N.; Zhao, Y. Experimental Test on Nonuniform Deformation in the Tilted Strata of a Deep Coal Mine. *Sustainability* **2021**, *13*, 13280. [CrossRef]
38. Li, M.; Lv, H.; Lu, Y.; Wang, D.; Shi, S.; Li, R. Instantaneous discharge characteristics and its methane ignition mechanism of coal mine rock damage. *Environ. Sci. Pollut. Res.* **2022**, *29*, 62495–62506. [CrossRef]
39. Yu, W.; Li, K.; Liu, Z.; An, B.; Wang, P.; Wu, H. Mechanical characteristics and deformation control of surrounding rock in weakly cemented siltstone. *Environ. Earth Sci.* **2021**, *80*, 337. [CrossRef]
40. Liu, T.X.; Peng, Z.B.; Han, J.T. Research of simulation testing of Limestone's lithology. *Chin. J. Undergr. Space Eng.* **2005**, *6*, 878–881.